Low temperature synthesis of multiwalled carbon nanotubes and incorporation into an organic solar cell

Kudzai Mugadza, Vincent O. Nyamori, Genene T. Mola, Reuben H. Simoyi & Patrick G. Ndungu

Taylor & Francis
Taylor & Francis Group

Low temperature synthesis of multiwalled carbon nanotubes and incorporation into an organic solar cell

Kudzai Mugadza[a], Vincent O. Nyamori [ID][a], Genene T. Mola[a], Reuben H. Simoyi[a] and Patrick G. Ndungu [ID][b]

[a]School of Chemistry and Physics, University of KwaZulu-Natal, Durban, South Africa; [b]Department of Applied Chemistry, University of Johannesburg, Johannesburg, South Africa

ABSTRACT

Metal nanoparticle (MNP) catalysts used for the synthesis of multiwalled carbon nanotubes (MWCNTs) consisted of single metals (Fe, Ni or Co) and bimetallic mixture (CoFe, NiFe or NiCo). MWCNTs were successfully synthesised at 200 °C in 10 min using liquefied petroleum gas as carbon source with non-equilibrium plasma enhanced chemical vapour deposition (PECVD) method. The nanostructures and the morphology of the MNPs and the MWCNTs film were characterised using relevant microscopic and spectroscopic methods. The synthesised MWCNTs were used as part of the electrode material in organic solar cell (OSC) set-up. Poly (3,4-ethylenedioxythiophene): polystyrene sulfonate (PEDOT: PSS) was used as an electron transporter and poly-3-hexyl thiophene (P3HT) as an electron donor. The performance of OSC devices was tested using standard electrical measurements and solar simulator operating at 100 mW/cm^2. The measured power conversion efficiencies was found to be dependent on the metal catalyst used during synthesis. Among all the catalysts employed in this investigation, the best device performance was found from the synthesis of MWCNTs using Fe as a catalyst followed by Co and then Ni, respectively.

1. Introduction

Technological advancement and population growth has brought about a huge demand for energy globally [1–3]. Renewable sources of energy are seen as viable alternatives in an effort to meet the growing energy demand, as well as to reduce greenhouse gas emissions and other deleterious environmental effects which occur from using fossil fuels. Amongst the possible renewable sources; solar energy is considered as an inexhaustible and relatively clean source of energy. Considerable and continual efforts to utilise this sustainable energy supply has been a global focus for the last few decades [2–4]. This includes development of modified energy storage and conversion devices such as batteries [5], super capacitors [6], light emitting diodes (LEDs) [7], and solar cells [2,3,8].

There are several types of solar cells available for the conversion of solar energy to useful electricity depending on the material used and device fabrication. These include dye sensitised solar cells (DSSC) [9], inorganic and organic solar cells (OSC) [2,3,8,10], and various other hybrid systems [2,3]. Widespread and most commercially successful systems are inorganic solar cells; specifically silicon based, and these can be monocrystalline [11], polycrystalline [12], or amorphous [13]. These types of solar cells are made from very reliable and advanced processing technologies, and have been reported to have relatively high efficiency rates [2,14]. However, the fabrication techniques of these devices can be very expensive as they require huge labour and investments on the requisite facilities [10]. On the other hand, solar cells fabricated from organic semiconductor materials are likely to be much cheaper since they can be potentially assembled using current polymer processing technologies, and such systems can take advantage of the inherent advantages associated with polymers in terms of construction, design, aesthetic appeal, and flexibility in application [2]. However, to date, solar cells made from organic semiconductor polymers are less efficient than inorganic systems, and are prone to environmental degradations [2,3,8]. In an effort to improve the suitability of semiconductor polymers for device fabrication, small organic or inorganic molecules or a combination of both, with or without incorporation of nanomaterials have been employed [15]. One very promising type of nanomaterial that has been used in OSCs are carbon nanotubes [2,8].

The use of carbon nanotubes in OSCs has been recently reviewed [2,8]. In addition, we recently reported on the synthesis of boron and nitrogen doped multi-walled carbon nanotubes, and the assembly of OSCs using doped nanotubes [16–18]. Multi-walled carbon nanotubes (MWCNTs) may improve the performance of organic solar cells by enhancing electron-hole dissociation [2,8,19], improving the mobility of charge carriers by providing highly conductive pathways [17,20–22], and may enhance the environmental stability of OSCs [16,17,22]. However, one of the main challenges with incorporating MWCNTs in OSCs is the random orientation of the nanotubes within the overall assembly. Randomly oriented MWCNTs can extend across the photoactive layer and result in problems such as shunting of some of the generated charge carriers [18,19,23]. Vertically aligned MWCNTs are associated with improved electrical conductance [24]. This is attributed to the ability of the internal walls of the vertically aligned nanotubes to participate in electrical transport without cross linkage problems [24]. The use of vertically aligned MWCNTs may provide the advantages of nanotubes without the disadvantage of overextension across the photoactive layer. In addition, the use of vertically aligned MWCNTs can maximise surface area and therefore enhance overall cell performance.

The main method used for the synthesis of MWCNTs, both on a lab-scale and commercially, is the thermal chemical vapour deposition (CVD) [25,26]. The thermal CVD technique utilises high temperatures in the range 500–1100 °C [2,25–27]. These temperatures are not suitable for the direct growth of vertically aligned MWCNTs onto substrates, especially when considering using substrates with very low strain points or thermal stabilities below these high temperatures. However, among the modified CVD methods developed, the plasma-enhanced chemical vapour deposition (PECVD) has proven to be favourable in overcoming such shortcomings. This method makes use of the plasma which can produce the relevant active species from a suitable carbon source and enables suitable growth of CNTs directly on the substrate. However, a limited number of studies have been done on the production of CNTs which are vertically aligned and dense, and

grown directly on the substrate using lower temperatures. Therefore, in this study we investigate the growth and physical-chemical properties of carbon nanotube arrays directly on the substrate for application in organic solar cells. We investigated synthesis temperatures as low as 200 °C with the minimum possible deposition time, 10 min, using non-equilibrium PECVD method. Furthermore, we investigated the effect of different catalysts, monometallic and bimetallic catalysts, on the performance of the organic solar cells.

2. Experimental

2.1. Materials

All chemicals and gases used in these experiments were obtained from commercial sources and were used as received without further purification. These included: Acetone 100% (AR), Protea Chemicals, South Africa; ammonium solution 25% (CP), Associated Chemical Enterprises, South Africa; cobaltous chloride 99% (AR), Rochelle Chemicals, South Africa; hexadecylamine (HDA) 90% (technical), Capital Lab Supplies, South Africa; iron chloride hexahydrate 99% (AR), Associated Chemical Enterprises, South Africa; Isopropanol 99.5% (AR), Saarchem, South Africa and nickel chloride hexahydrate 98% (AR), Saarchem, South Africa. All gases used were purchased from Afrox, South Africa. This included argon (ultra high purity) and liquefied petroleum gas. A $30 \times 30 \times 0.7$ mm ITO (15 Ω) glass was purchased from Luminescence Technology Corp, Taiwan.

2.2. Methods

The methods employed in this work were divided into three stages i.e. catalyst synthesis, MWCNTs synthesis and application of the synthesised MWCNTs in solar cells.

2.2.1. Synthesis of catalysts

The synthesis procedure was based on modification of a method used by Choi and co-workers [28]. In brief, HDA (0.5 g) was dissolved in acetone (25 mL). The mixture was ultra-sonicated for 20 min until a homogeneous mixture was obtained, then stored in a beaker for further use. In a separate 100 mL beaker, $FeCl_3.6H_2O$ (1.352 g) was dissolved in 50 mL of deionised water. The solution (20 mL) was transferred into a three-necked round-bottomed flask. The mixture was ultra-sonicated for 5 min and thereafter placed onto a hot plate. To the mixture, an NH_4OH (20 mL) solution was added dropwise. The pH of the solution was maintained at 11, with the dropwise addition of the precipitating agent (NH_4OH) while heating the solution at 80 °C under vigorous stirring (300 rpm). The precipitation temperature was maintained constant within ± 1 °C using an oil bath. After 10 min, the prepared HDA/Acetone solution (5 mL) was added dropwise for 5 min while stirring. An additional NH_4OH (5 mL) was added and then the solution was further stirred for 5 min. Thereafter, four aliquots of HDA/Acetone solution (5 mL) were added at 5 min interval. After the addition of the last aliquot of HDA, growth was allowed for 30 min, at a constant temperature of 80 °C. The mixture was consistently stirred during this step in order to produce a stable suspension. This was followed by cooling the contents in a round-bottomed flask to room temperature under running water. The precipitates were centrifuged

at 2500 rpm for 20 min, then sequentially and thoroughly washed with ethanol (6 mL) and acetone (10 mL) several times, until a colourless supernatant was obtained (an indication of total removal of the excess surfactant). The final product was stored as a concentrated mixture in a refrigerator at temperatures below 5 °C to avoid fusion of the particles. The procedure was repeated for Co and Ni catalysts. The same procedure was followed for the bimetallic catalysts, CoFe, NiFe and NiCo. The metal chloride salts were dissolved in deionised water as individual solutions.

2.2.2. Synthesis of MWCNTs

Non-equilibrium PECVD apparatus was constructed with commercially available consumables. A simple schematic diagram is shown in Figure 1.

The system consists of an Electrical Supplies Corporation alternator, 0–260 V set at 110 V. The plasma driver, model PVM/DDR, was connected to the alternator. The plasma driver was connected with two 4 mm thick electrical wires which were in turn connected to a 10 mm × 3 mm × 2 mm copper foil. Two full trough infra-red ceramic heaters from Unitemp were connected to an RKC FJ02 temperature controller which was connected to a J-type thermocouple. The reactor vessel was a quartz tube with a diameter of 40 mm and a length of 25 mm. The system was closed by connecting the gas and plasma inlet to one end and to the other end was the gas exhaust. The gas flow rates were controlled using Swagelok variable area flow meters, VAF-G4-04S-1-0.

In this procedure, the synthesis temperature was maintained at 200 °C for 10 min using LPG (liquid petroleum gas) gas as the carbon source, while Ar, in all cases, was constantly used as the inert atmosphere. The flow rates of the two gases were kept at a ratio of 3:1 for the carbon source to the inert atmosphere, respectively. Other gases were tested in the
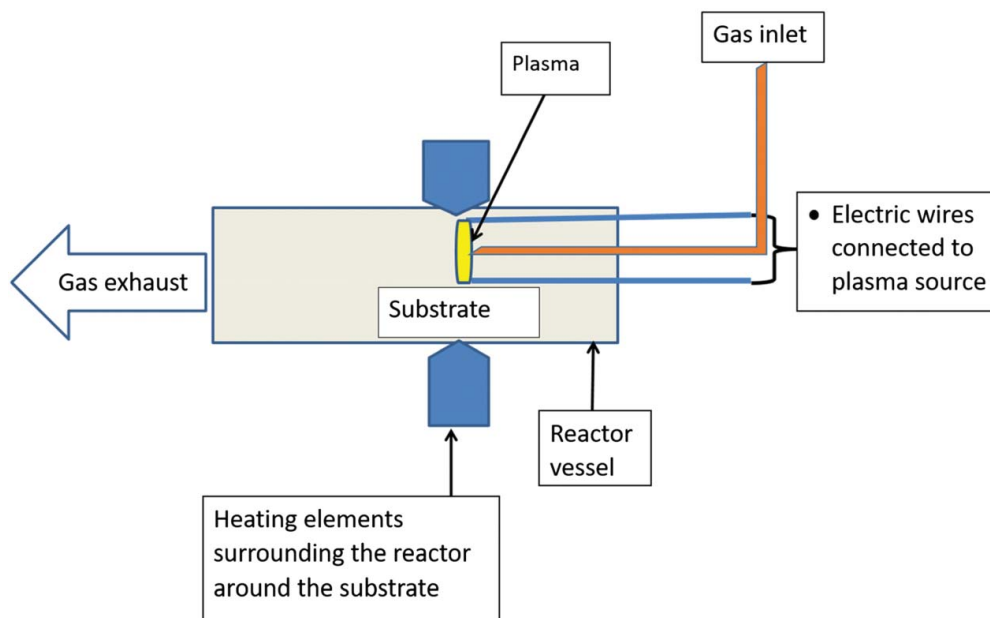

Figure 1. Schematic illustration of the non-equilibrium PECVD.

PECVD setup, and these were ethylene and methane. The synthesis procedure was carried out in two stages; i.e. substrate preparation and CNT synthesis.

An indium tin oxide (ITO) coated glass (thermal stability, 666 °C) was used as the substrate. The ITO glass substrates were cleaned and part of ITO etched to give a non-etched and etched partition, with ratio of 1:3:2 to get 5:15:10 mm division. The ITO was protected from etching by covering the conductive sides with insulation tape which covered an area of 20×20 mm^2. A 200 mL acid solution containing HCl: H$_2$O:HNO$_3$ in the ratio 12:12:1, respectively, was prepared. The prepared acid solution was heated to 70–90 °C on a hotplate. The ITO substrate (with masked areas) was placed in the solution for 60 s to etch the uncovered part. After etching the ITO substrate was rinsed under running tap water to dilute and remove excess acid. The covering insulation tape was then removed and the substrate was ultra-sonicated in a mixture of a detergent and distilled water for 10 min. This was followed by the thorough cleaning of the substrate with a cotton ball and acetone. The substrate was then rinsed in pure deionised water to remove the detergent and further ultra-sonicated for 10 min. The substrate was then ultra-sonicated in acetone for another 10 min and further ultra-sonicated in isopropanol for an additional 10 min. The substrate was left to dry in an oven at a temperature of 120–150 °C for 30 min until complete dryness was achieved.

The MNPs prepared were diluted and drop dispersed, 10 µL of respective metal nanoparticle, 1 mg/mL in ethanol using a micro pipette. The MNPs were spread onto the conductive side of the hydrolysed ITO glass substrate covering the 15×15 mm^2 area in the centre of the substrate. The other 5×5 mm^2 and 10×10 mm^2 ends of the conductive and non-conductive sides, respectively, were left to be electrode materials. The ITO substrate with MNPs was placed at the centre of the reactor vessel in the non-equilibrium PECVD set-up. To remove the air, the system was flushed with the Ar gas for 5 min then purged with the carbon source for another 5 min. The radio frequency plasma driver was set at 50 W. The current of the plasma was 0.3 A. The substrate was heated up to the synthesis temperature, 200 °C, under Ar flow, at a flow rate of 100 mL/minute, before reducing the Ar flow. The power supply was turned on and the current knob adjusted to initiate the plasma. Once the plasma was stable (about 2 min), the hydrocarbon source was slowly increased to a flow rate of 300 mL/minute for 10 min. Thereafter, the hydrocarbon flow was terminated and the Ar flow was ramped up. The power supply and the plasma were switched off and the system cooled under Ar flow. In terms of characterisation, two approaches for analysis were used, i.e. (i) sample including substrate and (ii) sample without the substrate.

2.2.3. OSC device preparation

Bulk heterojunction organic solar cells (BHJ-OSCs) were fabricated on ITO coated glass substrate. The MWCNTs were deposited on the ITO side of the substrate for device fabrication. The photoactive layer, composed a mixture of poly-3-hexyl thiophene (P3HT), and phenyl-C$_{61}$-butyric acid methyl ester (PCBM) was prepared in chloroform solvent and sonicated for 3 hours to increase the miscibility of the molecules. The hole transport layer layer poly(3,4-ethylenedioxythiophene): poly styrenesulfonate (PEDOT:PSS) was spin casted on MWCNTs synthesised ITO substrate at 3000 rpm for 50 s. After spin coating the substrate was annealed at 120 °C for 10 min in an oven. The active layer P3HT:PCBM was spin-coated at 1500 rpm for 30 s, and then annealed again for 20 min at 120 °C. Finally, 0.6 nm

thick lithium fluoride (LiF) buffer layer and aluminium electrode (60 nm) were thermally evaporated in vacuum at 2.22×10^{-7} mbar using HHV Auto 306 vacuum evaporator equipped with INFICON SQM-160 thin film deposition thickness and rate monitor.

2.3. Characterisation

The structure, dimensions and topography of the MNPs and the MWCNTs were investigated by the use of transmission electron microscopy (TEM). A JEOL JEM 1010 model was used with a Mega view 3 camera attached. The MNP samples were prepared by diluting the catalyst solution, a pipette drop in 1 mL acetone and ultra-sonicated for 5 min at room temperature. A lacey or holey carbon-coated copper grid was dipped into the diluted solution and dried under a halogen lamp for 5 min. The grid was placed on the sample holder, loaded into the TEM, and images were taken at different magnifications from 80 000X-600 000X using a Mega view 3 camera. The particle sizes and MWCNTs diameter were determined using image J® software. A minimum of 100 particles or tubes were used for statistics.

Fourier transform infrared spectroscopy (FTIR) characterisation was performed using a KBr pellet disk and an FTIR spectrometer (Perkin Elmer Spectrum 100 instrument). Dry potassium bromide (150 mg) powder and 2 mg of respective sample were ground using a motor and pestle. The mixture was pressed into a pellet using 10 Tons of pressure for 2 min in a ring press model 00-25 supplied by Research Industrial Company, England. The CO_2 absorption in the background was removed by air scanning. The resolution used was 4 cm^{-1}, in a spectral range of 4000-400 cm^{-1}.

Thermal stability, residual metal and the organic content analysis was confirmed by using a TA Instrument Q series^{TM} Thermal Analyser TGA (Q600). The measurements were done in air at a flow rate of 50 mL/min from ambient temperature to 1000 °C. The isothermal time was 1 min with a ramp temperature of 10 °C/min. To acquire the data, a TA instruments Universal Analysis 2000 software package was used. Weight loss curves were re-plotted using Origin® software.

The carbon products were analysed with a Raman spectrometer; model Delta Nu Advantage 532^{TM}. The grating lines were 1800 per mm. The laser excitation wavelength was 532 nm and the power generally used was medium high according to the software of the instrument. Integration time of 45 s and a resolution 10 cm^{-1} was set. Spectral analysis was done using an average of three spectra for each MWCNT sample. Background smoothening and baseline correction was done by using the Software 2D CCD detector provided with the Raman instrument.

Current-voltage characterization was determined by using standard solar simulator model # SS50AAA (Pet Photoemission Tech. Inc.), with a Keithley 2420 source meter. Where the simulator was operating at AM 1.5 and the power input was 100 mW/cm^{-2}.

3. Results and discussions

3.1. Catalysts

The synthesised MNPs were characterised mainly using SEM and TEM for surface morphology and TGA for residual metal content as well as the determination of the presence

of the organic coating. During synthesis, the colloidal solutions were maintained at a pH of ≈11. This optimum pH was based on a study by Mahdavi *et al.* in which iron oxide nanoparticles were synthesised [29]. The group used iron chloride hexahydrate and tetra-hydrate precursors, and applied the co-precipitation method. From their finding they concluded that particle size of the nanoparticles relied on pH, where, nanoparticle sizes would reduce in size with increasing pH, i.e. from pH8 to pH11 and increased with pH rise i.e. from 11 [30]. Herranz *et.al.* also suggested that a pH of 11 is capable of maintaining the molar ratios of the precursors under a non-oxidative environment [31]. The reaction temperature was maintained at 80 °C since the surfactant was added from the beginning of synthesis. Therefore, this temperature would be suitable to assist the prevention of any potential intermediate complexes to form [32,33]. During the course of the reaction, a vigorous agitation was necessary to help dispersion by inhibiting nanoparticle growth and surface attractions that could lead to agglomeration of the nanoparticles. The surfactant, HDA, was added as aliquots to the metal chloride and ammonia solution such that the surfactant would be able to enclose the surface of the MNPs [34]. The first aliquot of HDA acted as the primary surfactant whilst additional aliquots acted as the secondary surfactant. These aliquots had different effects on the growth of the nanoparticles. The polar heads of the first surfactant are bound to adsorb onto the MNP catalyst particles and the nonpolar tails are left floating in the solvent system [34]. Van der Waals forces are responsible for the interaction between the additional aliquots of the surfactant and the first surfactant aliquot. The tails of the first surfactant that are left floating around in the solvent system then bind with the nonpolar tails in the additional surfactant. The interaction leaves the polar heads to be solvent and ammonia bound [28]. Hou *et al.* synthesised Ni nanoparticles using Ni(acac)$_2$ precursor and HDA and triocytylphosphine oxide as surfactants to control the metal size [35]. They reported that growth of the resulting oxide was dependent on HDA, smaller Ni nanoparticle diameters were related to the addition of HDA.

3.1.1. *TEM*

TEM analysis was used to determine the actual size and structure of the MNPs.

The images in Figure 2 show that the metal nanoparticles of Fe (a) and CoFe (d) had spherical shapes, while those from Co and Ni had shapes that looked like irregular and elongated spheres. From the size distribution histograms (Figure 2), all nanoparticles synthesised were well dispersed and showed uniform sizes. There is no noticeable difference between the images of single and bimetallic catalysts. All the nanoparticles show a narrow size distribution in the range of 3–10 nm with a good dispersion. This suggested that HDA played a key role as a surfactant as well as the reducing agent as reported in literature by Li *et al* [34]. The metal precursors were reduced from +3, or +2 (Fe, Co and Ni) to their respective zero valence oxidation states. However, the MNPs may have formed metal oxides/hydroxides phases through air oxidation, since the synthesised MNPs are expected to have relatively large surface areas which can enhance oxidation [36].

This observation was also noticed on EDX spectra, Figure 3, with the presence of oxygen (O) signal.

Generally, the EDX spectra for single metal catalysts showed atomic weight % ratio of the metals with the carbon in a 1:1 ratio. The EDX spectrum for bimetallic catalysts showed that atomic weight % ratios corresponded with the expected molar ratios of the
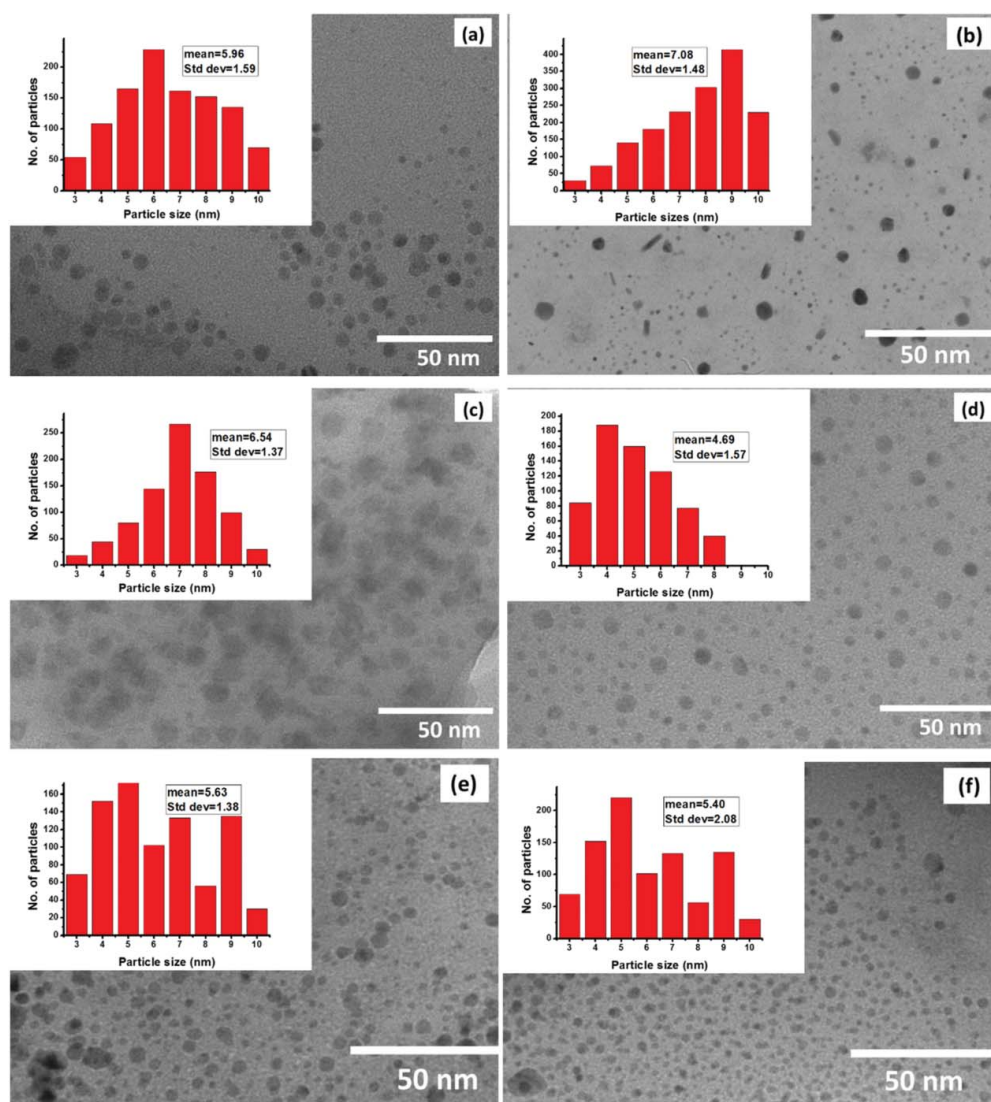
Figure 2. TEM images and inserts of the histograms of metal nanoparticles; (a) iron, (b) cobalt, (c) nickel, (d) cobalt-iron, (e) nickel-cobalt and (f) nickel-iron.

mixed metals for instance, Co to Fe stoichiometric ratios in the CoFe MNPs spectrum was 1:2. The signal from carbon (C) was attributed to the organic coating (HDA) around the surface of MNPs. HDA acts by forming co-ordination complexes with the metal ions in the solution. The amine head surrounds the nanoparticles formed thus reducing sintering [37]. To further understand the role of HDA and the chemical environment of the final product, FTIR analysis was done.

3.1.2. FTIR spectroscopy
FTIR spectroscopy was used to determine the vibrational and stretching frequencies of the functional groups present in the synthesised MNPs. The formation of the MNPs, through
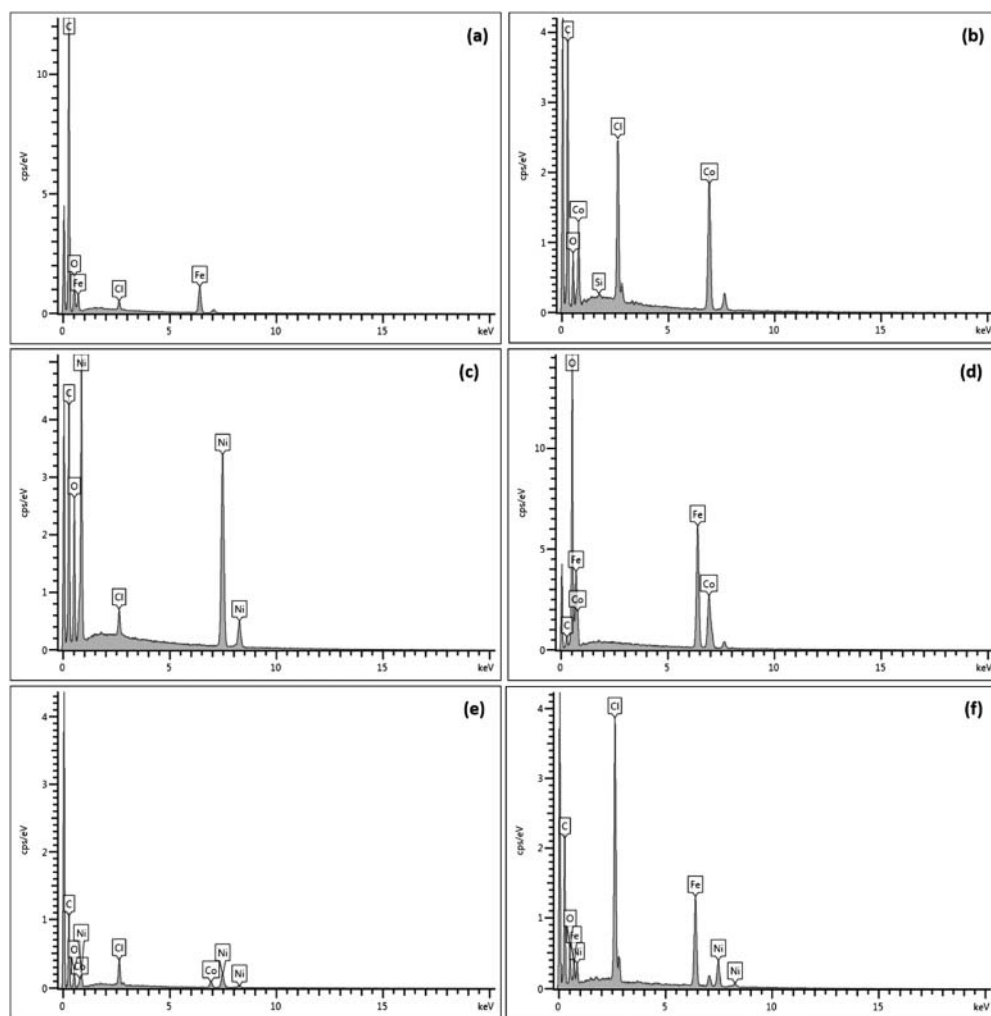
Figure 3. EDX images of synthesised metal nanoparticles (a) iron, (b) cobalt, (c) nickel, (d) cobalt-iron, (e) nickel-cobalt and (f) nickel-iron.

the interaction between the surfactant and the MNPs, was thus further confirmed. A stacked image showing all the MNPs with HDA are provided in Figure 4.

The FTIR spectra of the mixture of HDA and the synthesised MNPs showed that there were some interactions between the surfactant, HDA, and the MNPs. In MNPs containing cobalt, a peak between 3500 and 3700 cm^{-1} was attributed to free O-H groups [38]. It was speculated that the O-H stretch of the Co samples was attributed to the fact that Co containing samples are highly hydroscopic hence, samples containing Co had trace amounts of OH. The N-H stretching band at 3331, 3554 and 3172 cm^{-1} showed a redshift with the synthesised metal nanoparticles. This peak shift indicates that the HDA amine group has bound to the surface of the MNPs [39,40]. The C-H stretching 2917 cm^{-1} (symmetric) and 2848 cm^{-1} (anti-symmetric) appeared at 2916 and 2849 cm^{-1} respectively. This also could suggest that HDA had interacted with the MNPs [41]. The peak shifts in these oxide
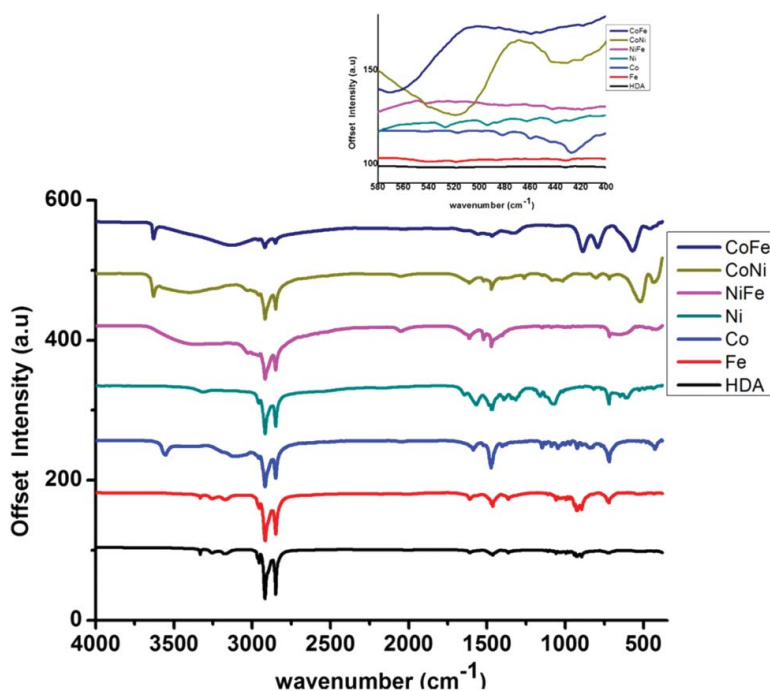
Figure 4. Comparison of the IR spectra of HDA and co-precipitation synthesised MNPs with the insert of the magnified 400–580 cm^{-1} region.

Table 1. Summary of FTIR peaks assigned to the co-precipitation synthesised metal nanoparticles [37,43,44].

Catalyst	Wavenumber (cm^{-1})	Assignment
Fe	422	Fe-O
Co	516, 481	O-Co-O
Ni	439	Ni-O
CoFe	570	Ferrite MNPs
NiCo	519	Cobaltite MNPs
NiFe	542, 418	Ferrite MNPs

molecules are mostly attributed to the constraint of the capping molecular motion which supposedly resulted from surface attachment of the HDA. The peak intensities had differences between the spectra. This was also postulated to be as a result of the HDA molecule on the MNPs forming a relative close-packed HDA layer which constrained the molecular motion [42]. Table 1 shows how bands of interest were assigned on individual MNPs.

FTIR gave characteristic metal-oxide peaks. To further determine the amount of the metals and the amount of the surfactant present in the MNPs, TGA analysis was done.

3.1.3. Thermogravimetric analysis

The various samples were analysed using TGA. The general trend of all the MNPs synthesised using the co-precipitation method showed that the TGA curves had five different steps. A stacked TG curve is shown in Figure 5 where all MNPs are presented.
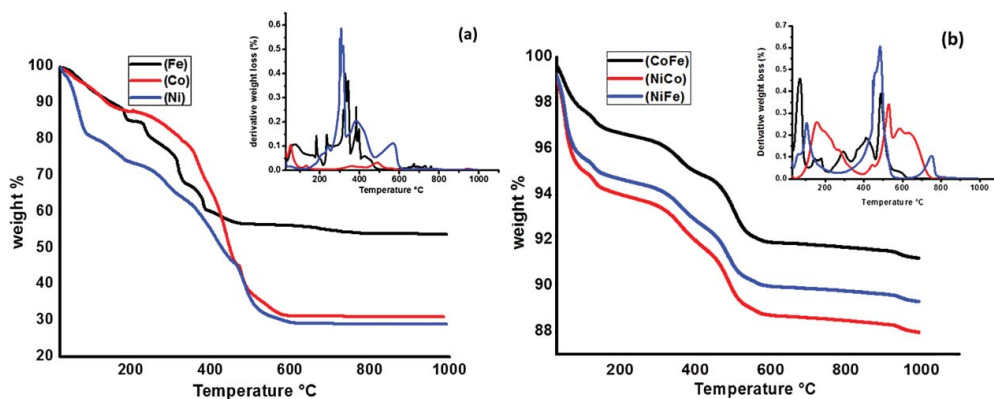
Figure 5. TGA curves of all the metal nanoparticles in air; (a) single metals and (b) mixed metals.

The TGA of the samples were run under air, and Figure 5 shows a small mass loss below 150 °C which was attributed to the release of adsorbed water. There was a second and third step around 200 and 375 °C, respectively, attributed to desorption and decomposition of the surfactant, carbon formation, as well as the removal of the unbound HDA on the surface of the metal nanoparticles. Further weight loss around 500 °C was due to de-hydroxylation of the surface and removal of some of the lattice residual HDA. This weight loss suggests that the interaction between the metal nanoparticles and the surfactant was strong. The final weight loss in the TG curve was observed at temperatures around 580 °C. This signified the termination of weight loss associated changes [44]. A dip around 900 °C was observed and this was attributed to the formation of different bimetallic phases that are not stable, i.e. decompose with an increase in temperatures [45]. The derivative weight loss percentage curves were plotted for each metal sample as shown Figure 5 inserts. In these derivative curves, it can be observed that as the thermal events progressed, there was a variation in the weight as a function of temperature. Therefore, the TGA results agreed with the FTIR results in showing the presence of the organic coating. The TGA curves show that weight loss was 72, 70 and 45% for Ni, Co and Fe respectively, then 12, 11 and 9% for NiCo, NiFe and CoFe respectively. Therefore, the single MNPs contained more of the organic coating than the mixed MNPs. The differences of the metal residual content were attributed to the differences in the MNP morphology and surface properties. Additionally, as observed from EDX, the monometallic nanoparticles contained atomic C in greater proportion than in bimetallic catalysts, hence, the difference in the metal residual content was also assumed to be due to the observed difference. In another study, Cao et al., suggests that the shape variation of the metal nanoparticles plays a significant role on their respective thermal properties [46]. Therefore, since the metal nanoparticles had almost the same sizes with slight differences in their shapes, the observed differences in their thermal stabilities can be attributed to their size and surface variations.

3.2. MWCNTs synthesis

The non-equilibrium (PECVD) approach was employed to overcome the high temperature problem associated with the thermal CVD. The role of plasma was to ionise the

gaseous feedstock under low temperatures [47]. The system was optimised in terms of the reaction temperature, time, plasma flame and the deposited CNT layer. In order to preserve the properties of the ITO coated glass substrate, Wang and Moore suggested employing low temperatures [48], hence a purpose built non-equilibrium PECVD apparatus was utilised. Another study by Ren *et al*. for synthesis of CNTs on glass substrate, showed that glass electrical resistivity increases by annealing up to 100 °C and decreases above 100 °C [49]. Therefore, temperatures below 300 °C were selected as ideal for the direct deposition of the MWCNTs on ITO glass substrate. The ITO substrates were placed directly below the plasma discharge to maximise the interactions between the plasma and the catalyst as suggested by Somers *et al* [50]. Since the physicochemical properties of the plasma and the catalyst can be modified by their co-existence [51].

Attempts to use gases such as methane and ethylene as the carbon sources resulted in the plasma flame being extinguished. This was attributed to the differences in the density and vapour pressures of the gases, and the ionisation and dissociation energies. The ignition source would not have been able to provide enough energy to initiate a cascade with the gases thus, the gases requires higher synthesis temperatures which can be above 350 °C [52]. Therefore, in this study LPG as carbon source and the co-precipitation synthesised MNPs as catalysts where investigated.

3.2.1. SEM analysis of the MWCNTs

The as synthesised MWCNTs using different catalysts were viewed under SEM using exceptionally low magnifications to investigate the alignment. Figure 6 shows the variations in the observed structures upon varying catalysts using low magnification.

Similar images were observed with respect to the different catalyst utilised. The SEM images (Figure 6) showed vertically aligned MWCNTs were successfully synthesised. Amorphous carbon material was observable from the aerial and side views (Figure 6). Besides this, no other distinctive observations were noticeable in both mono- and bi-metal catalysts from SEM images. EDX data confirmed the presence to the respective catalysts and carbon in the samples. The EDX spectra in the different catalysts observed showed the peaks of the respective catalysts. The Si, In, Sn and O_2 peaks were also present and they were assigned to the ITO coated glass substrate components.

3.2.2. TEM analysis on MWCNTs

To further characterise in terms of dimensions of the MWCNTs samples, TEM was utilised. Figure 7 shows hollow tubular nanostructures with thick walls from all the catalysts used.

This means the vertically aligned nanostructures observed by SEM analysis were MWCNTs (Figure 6). In some TEM images the catalyst nanoparticles were observed at the tip end, sides and inside the tube (Figure 7). Slightly noticeable size differences were observed with TEM images which showed different MWCNTs dimensions with respect to catalysts used. The alignment was attributed mainly to the plasma. The plasma contains positive ions in the cathode sheath. The plasma is responsible for the attracting the MWCNTs to follow a growth towards the source of the ions [53]. To some extent, van der Waals interactions between adjacent MWCNTs could also explain the alignment [54]. The least tube diameters where achieved with Fe as single catalyst whilst for bi-metal catalyst it was with CoFe. The differences in the mean diameters were attributed to the
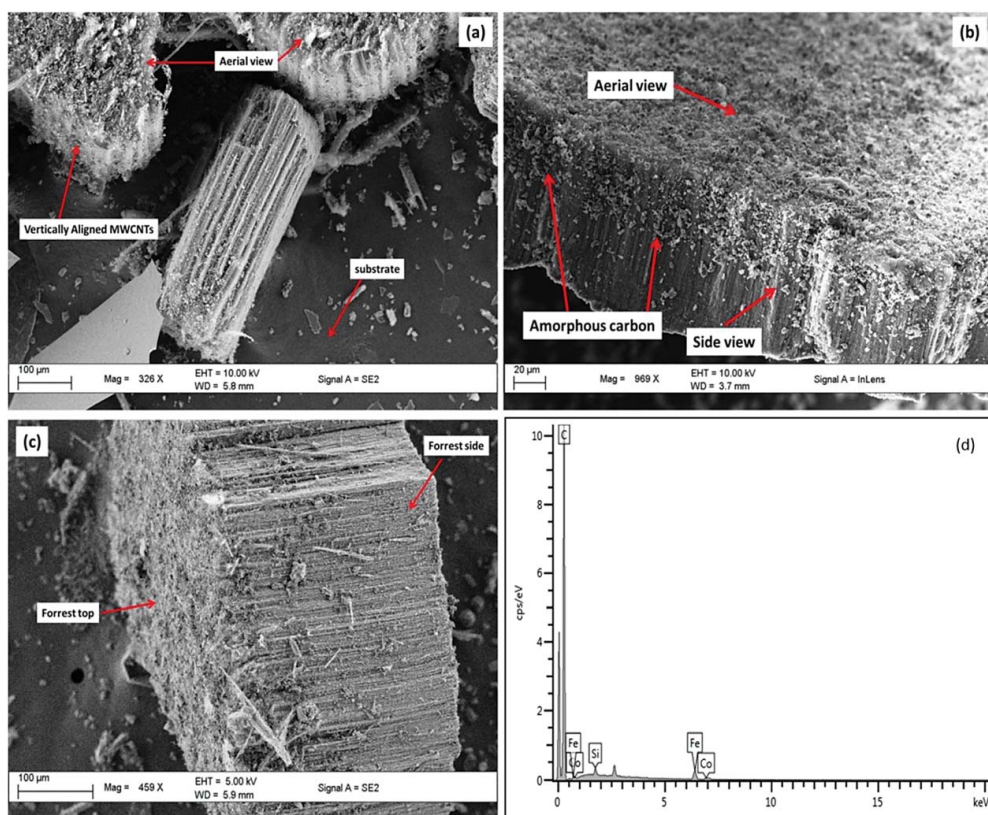
Figure 6. Representative images indicating the different views of the MWCNTs as observed using SEM for CoFe catalyst; (a) aerial view on substrate, (b) scrapped off aerial view (c) scrapped off side views and (d) the EDX spectrum.

variations in mean catalyst sizes observed [55,56]. Amongst mixed metal-catalysts, NiCo showed the largest CNT diameter and this could be explained using the austenite-phase concept where, Co and Ni are common Fe stabilising elements [57]. These austenite-stabilising elements are responsible for extending the austenite phase thus making the mixture of metals with Fe become more stable. It is this stability which is responsible for the enhanced carbon solubility in the mixtures containing Fe [57]. In the case of single metals, it is well known that transition metals have partially filled d shells. Therefore, this property enables interaction with hydrocarbons in order for catalysis to occur. Therefore, the electronic structure of these magnetites of Fe is responsible for catalysing the decomposition of the carbon source [58]. This suggests why Fe produced small diameter MWCNTs as compared to Co and Ni [59]. Raman analysis was done so as to determine the graphitic nature of the synthesised MWCNTs.

3.2.3. Analysis of the MWCNTs using raman spectroscopy

Raman analysis of the MWCNTs synthesised using the six catalysts showed characteristic CNTs disorder band (D band) and graphitic band (G band) as shown in Figure 8.
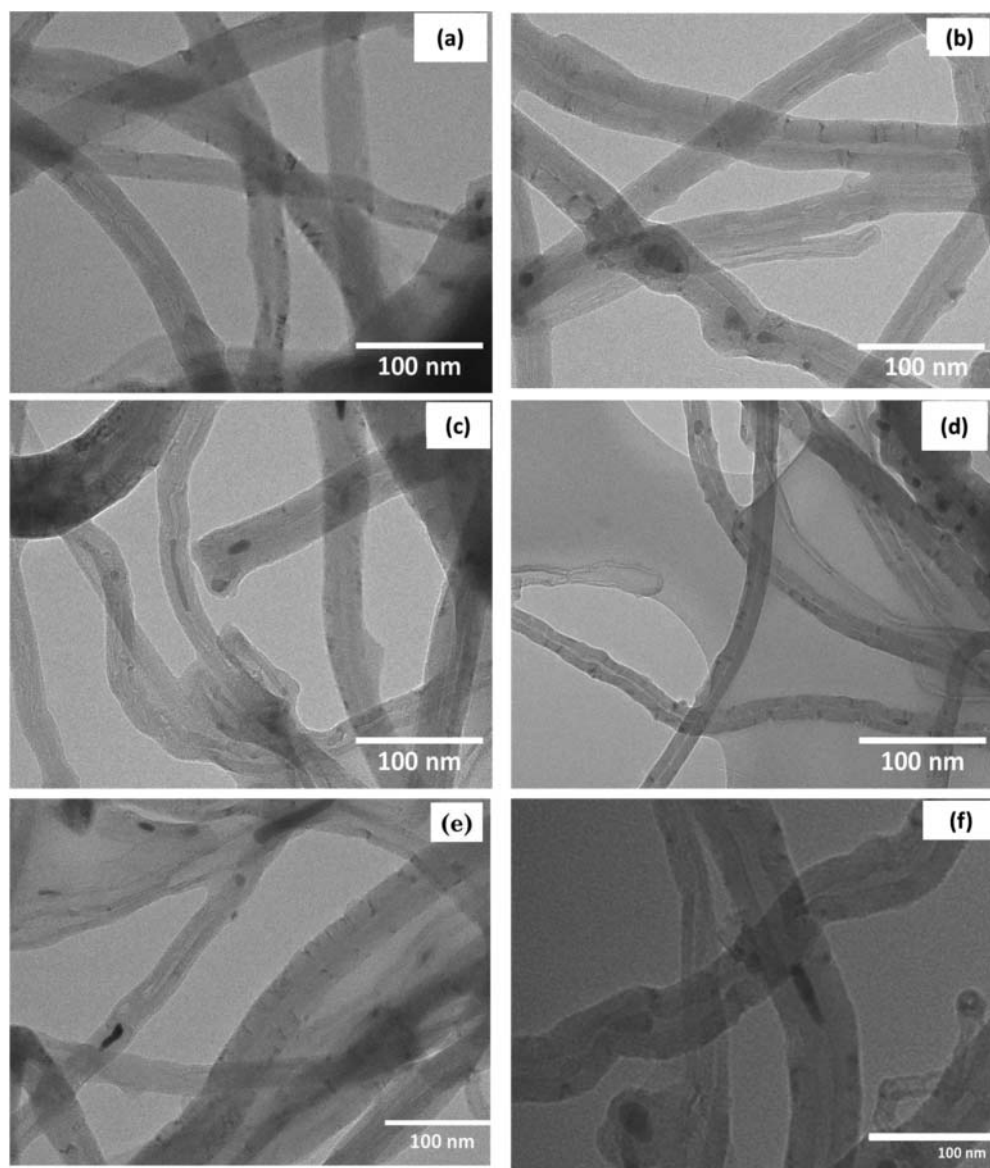
Figure 7. TEM images representing the various MWCNT structures synthesised where (a) Fe, (b) Co, (c) Ni, (d) CoFe, (e), NiCo and (f) NiFe are the respective catalysts used.

The D band due to defects is usually located at 1350 cm^{-1} and the G band, often associate with crystalline nature of the carbon atoms in the MWCNTs, at 1580 cm^{-1}[60]. The ratio of the D- to G- band (I_D/I_G) was calculated by dividing the areas under the respective bands. The results are presented in Table 2 for each catalyst.

Raman analysis showed that the MWCNTs with smaller mean diameters, from TEM analysis (Table 2), had higher I_D/I_G. When comparing the single metal catalysts, Fe had the least MWCNTs mean diameters and the highest disorder ratios. For mixed metal catalysts, CoFe had the highest disorder ratio. Therefore, the higher I_D/I_G ratios could be
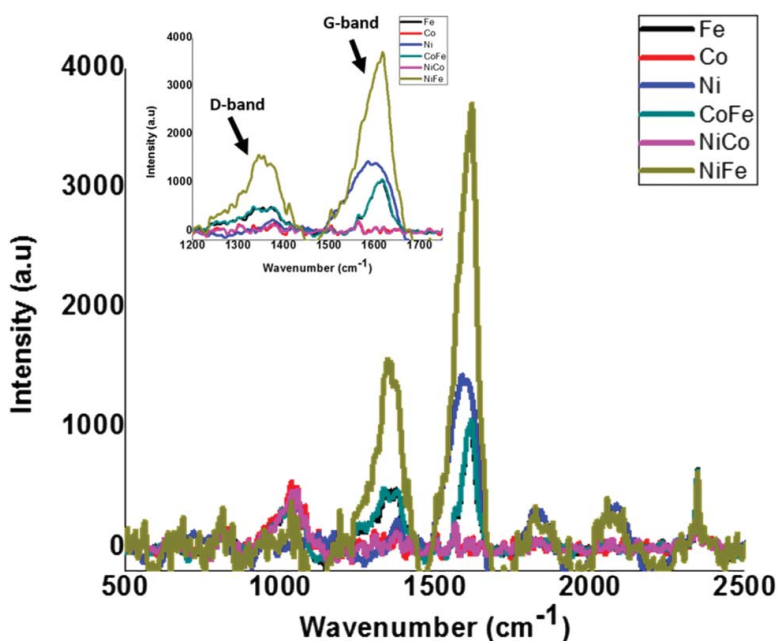
Figure 8. Raman spectra for the MWCNTs synthesised, the insert shows the position of the D-and G-band respectively.

Table 2. Comparison of the I_D/I_G in Raman analysis with respect to the MWCNTs diameters.

Catalyst	Mean tube diameter (nm)		Position (cm^{-1})		
	OD $\pm$ SD	ID $\pm$ SD	D-band	G-band	I_D/I_G
Fe	43 $\pm$ 5	6 $\pm$ 3	1373	1617	0.94
Co	65 $\pm$ 7	9 $\pm$ 2	1381	1620	0.73
Ni	56 $\pm$ 8	7 $\pm$ 5	1376	1585	0.92
CoFe	39 $\pm$ 9	5 $\pm$ 4	1334	1618	0.99
NiCo	45 $\pm$ 6	8 $\pm$ 2	1334	1600	0.85
NiFe	41 $\pm$ 5	6 $\pm$ 2	1350	1620	0.83

*OD: Outer Diameter, ID: Inner Diameter, SD: Standard Deviation.

attributed to greater carbon bond strains in the MWCNTs due to a low degree of crystallinity [60]. This may suggest that different metal catalysts as well as varying their combinations influence the nature of the MWCNTs produced. This ultimately affects the physical characteristics like tube diameters and hence their corresponding graphitic state. The characterisation techniques were substrate dependent; hence, no further investigations of the synthesised samples were further examined.

3.3. Assembly and characterization of a solar cell device

Bulk heterojunction organic solar cell (BHJ-OSCs) were fabricated on ITO coated glass substrate containing vertically grown MWCNTs. The active layer of the device is prepared
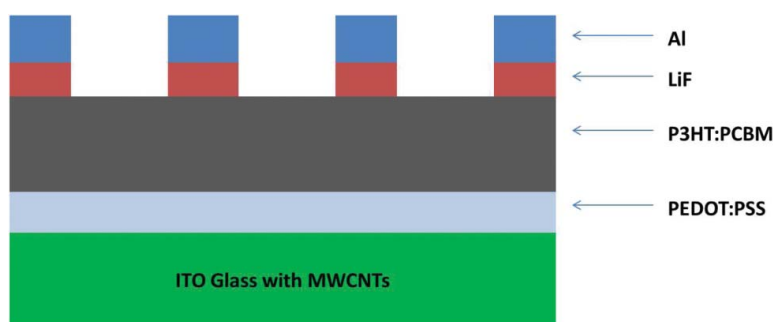
Figure 9. Schematic diagram of the layer arrangement in OSC.

in chloroform based solution containing P3HT and PCBM blend. Figure 9 illustrates a typical arrangement of the various layers of the device architecture.

The performance of the solar cells is determined in terms of device parameters which can be derived from the current-voltage characteristics (J-V) of each diode produced in a sample. Fill factor (FF) and power conversion efficiency (PCE) of the device are defined as:

$$FF = \frac{J_{Max} \times V_{Max}}{J_{sc} \times V_{oc}} \qquad (1)$$

$$PCE = FF \frac{J_{sc} \times V_{oc}}{P_{in}} \qquad (2)$$

J_{Max} and V_{Max} represent current density and voltage at maximum power point; J_{SC} represent short-circuit current density; V_{OC} is open circuit voltage and P_{in} stands for incident light power [61].

The J-V characteristics of the devices were measured both under dark and illumination conditions. Figure 10 shows the measured J-V curves taken from the various
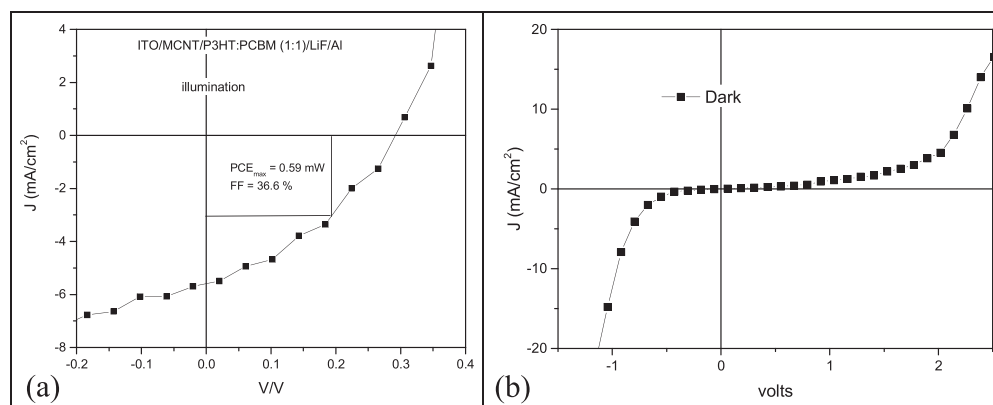

Figure 10. Comparison of current against voltage (J/V) plots in (a) illumination and (b) dark using MWCNTs prepared.

samples in these investigations. In these devices, some of the OSC diodes showed good device rectification behaviour while others showed good conductivity. We also have observed a number of diode showing no sign of device rectification because of Ohmic contact created by protruding MWCNTs between ITO and Al electrodes. The main reason for using vertically grown MWCNTs was to facilitate the charge transport process by sequentially filling the CNTs with hole transport layer PEDOT: PSS and the photoactive layer (P3HT:PCBM), respectively. Therefore, the good conductivity MWCNT is responsible for the improved electrical conductance due to their internal walls participating in the electrical transportation which enables large current-carrying capacity [24]. Preventive procedures of making the devices in a dark room were executed such that the PEDOT:PSS would not degrade [62]. This was so because when exposed to UV illumination the PEDOT:PSS disintegrates and initiates water into the active layer of the device and thus making it being slightly acidic. LiF/Al was used as the electron collecting contact. Figure 10 illustrates the current versus voltage (J/V) plots obtained using the MWCNTs synthesised using non-equilibrium PECVD with LPG as the carbon source.

Figure 10 is the current-voltage characteristics of the devices fabricated in the current investigations taken both under illumination and dark condition. Figure 10 (a) represents a device with largest fill factor of 37% and a power conversion efficiency of 0.59%. A good rectification behaviour of the diode can be seen in Figure 10 (b) at an applied bias of −0.6 V. Most of the samples tested under illumination provided some values of device parameters as presented in Table 3.

The highest V_{oc} and FF were observed for Co, but the highest J_{SC} and efficiency were observed for Fe. NiCo and NiFe had no FF and efficiency values due to constraints associated with series resistance. Several factors account for the series resistance and these include; the formation of insulator between active layer and the Al electrode, and also contact resistance and poor optimisation of the P3HT:PCBM film thickness [24]. The low efficiency could be due to the electronic nature of the respective catalysts in the synthesis of the MWCNTs as well as the formation of phase separated MWCNT cluster in the photoactive layer. The observed trend showed that in the single metal catalysts, Fe synthesised MWCNTs showed the highest efficiency, 0.68%, followed by Co and Ni, while a combination of CoFe showed better efficiency amongst the mixed metal catalyst. This could suggest that the catalytic nanoparticles were participating in the electronic transfer processes in devices. This was attributed to the size of the MNPs, the smaller the size the smaller the diameter of the MWCNTs [55,56]. Hence, for this case, the small sized MWCNTs are better electron transporters.

Table 3. Measured cell parameters for all MWCNT samples.

MWCNTs sample/catalyst	V_{oc} (V)	J_{sc} (mA.cm^{-2})	FF (%)	Efficiency (%)	Rectification
a (Fe)	0.17	15.62	25.96	0.68	Yes
b (Co)	0.29	5.59	36.53	0.59	Yes
c (Ni)	0.17	14.36	21.52	0.51	Yes
d (CoFe)	0.29	5.62	30.55	0.50	Yes
e (NiCo)	0.17	14.36	-	-	No
f (NiFe)	-	-	-	-	No

4. Conclusions

The MNPs obtained showed mono-dispersion with a narrow size distribution (3–10 nm). FTIR spectroscopy and TGA results confirmed the presence of the HDA in the final MNPs product. Hence, the MNPs were successfully coated with the amine groups of the HDA. The synthesised MNPs were used for synthesis of vertically aligned MWCNTs. MWCNTs were successfully synthesised using LPG as a carbon source at 200 °C in 10 min. Therefore, non-equilibrium PECVD was suitable for growing the MWCNTs directly on the substrate without destroying the substrate properties. The MWCNTs diameters depended on the size of the metal catalyst particles. This in turn affected the graphitic nature of the MWCNTs. All the metal catalyst synthesised MWCNTs were tested for their capability in OSC and it can be concluded that LPG synthesised MWCNTs are suitable electrode components. Also, catalytic nanoparticles used in the synthesis of the MWCNTs influences the ultimate activity of the MWCNTs in the OSC device. Accordingly, single metal catalysts exhibited best efficiencies as compared to bimetallic counterparts. The observation was attributed to the nature of the catalyst particles. However, all the samples produced low efficiencies when compared to literature.

Disclosure statement

No potential conflict of interest was reported by the authors.

ORCID

Vincent O. Nyamori http://orcid.org/0000-0002-8995-4593
Patrick G. Ndungu http://orcid.org/0000-0002-1454-8590

References

[1] Popp DC. The effect of new technology on energy consumption. Resource Energy Econ. 2001;23:215–239.
[2] Keru G, Ndungu PG, Nyamori VO. A review on carbon nanotube/polymer composites for organic solar cells. Int J Energy Res. 2014;38:1635–53.
[3] Yan J, Saunders BR. Third-generation solar cells: a review and comparison of polymer:fullerene, hybrid polymer and perovskite solar cells. RSC Adv. 2014;4:43286–43314.
[4] Solangi KH, Islam MR, Saidur R, et al. A review on global solar energy policy. Renew Sustain Energy Rev. 2011;15:2149–2163.

[5] Guoping W, Qingtang Z, Zuolong Y, et al. The effect of different kinds of nano-carbon conductive additives in lithium ion batteries on the resistance and electrochemical behavior of the LiCoO2 composite cathodes. Solid State Ionics. 2008;179:263–268.

[6] Caglar B. Production of carbon nanotubes by PECVD and their applications to supercapacitors [master's thesis]. Barcelona: Universitat de Barcelona; 2010.

[7] Zhang D, Ryu K, Liu X, et al. Transparent, conductive, and flexible carbon nanotube films and their application in organic light-emitting diodes. Nano Lett. 2006;6:1880–1886.

[8] Cataldo S, Salice P, Menna E, et al. Carbon nanotubes and organic solar cells. Energy Environ Sci. 2012;5:5919–5940.

[9] Mombeshora ET, Simoyi R, Nyamori VO, et al. Multiwalled carbon nanotube-titania nanocomposites: Understanding nano-structural parameters and functionality in dye-sensitized solar cells. South African J Chem. 2015;68:153–164.

[10] Mohammad Bagher A. Comparison of Organic Solar Cells and Inorganic Solar Cells. Int J Renew Sustain Energy. 2014;3:53.

[11] Choi SJ, Yu GJ, Kang GH, et al. The electrical properties and hydrogen passivation effect in mono crystalline silicon solar cell with various pre-deposition times in doping process. Renew Energy. 2013;54:96–100.

[12] Xue C, Rao J, Varlamov S. A novel silicon nanostructure with effective light trapping for polycrystalline silicon thin film solar cells by means of metal−assisted wet chemical etching. Phys Status Solidi A. 2013;210:2588–2591.

[13] Misra S, Yu L, Foldyna M, et al. High efficiency and stable hydrogenated amorphous silicon radial junction solar cells built on VLS-grown silicon nanowires. Solar Energy Mat Solar Cells. 2013;118:90–95.

[14] Green MA, Emery K, Hishikawa Y, et al. Solar cell efficiency tables (Version 45). Prog Photovolt: Res Appl. 2015;23:1–9.

[15] Somani PR, Somani Savita P, Umeno Masayoshi. Toward organic thick film solar cells: three dimensional bulk heterojunction organic thick film solar cell using fullerene single crystal nanorods. Appl Phys Lett. 2007;91:173503.

[16] Keru G, Ndungu P, Mola G, et al. Bulk Heterojunction Solar Cell with Nitrogen-Doped Carbon Nanotubes in the Active Layer: Effect of Nanocomposite Synthesis Technique on Photovoltaic Properties. Materials. 2015;8:2415.

[17] Keru G, Ndungu PG, Nyamori VO, et al. Charge extracting buffer layers in bulkheterojunction organic solar cell. J Mat Sci: Mat Elect. 2015;26:9891–9897.

[18] Keru G, Ndungu PG, Mola GT, et al. Organic Solar Cells with Boron- or Nitrogen-Doped Carbon Nanotubes in the P3HT : PCBM Photoactive Layer. J Nanomat. 2016;2016:1.

[19] Capasso A, Salamandra L, Di CA, et al. Low-temperature synthesis of carbon nanotubes on indium tin oxide electrodes for organic solar cells. Beilstein J Nanotechnol. 2012;3:524–532.

[20] Nismy NA, Jayawardena KDGI, Adikaari AADT, et al. Nano-engineering of hybrid organic heterojunctions with carbon nanotubes to improve photovoltaic performance. Organic Elect. 2015;22:35–39.

[21] Sahoo RK, Atta S, Singh NDP, et al. Influence of functional derivatives of an amino-coumarin/MWCNT composite organic hetero-junction on the photovoltaic characteristics. Mat Sci Semiconduct Proc. 2014;25:279–285.

[22] Singh V, Arora S, Arora M, et al. Optimizing P3HT/PCBM/MWCNT films for increased stability in polymer bulk heterojunction solar cells. Phys Lett A. 2014;378:3046–3054.

[23] Wang C, Gao E, Wang L, et al. Mechanics of network materials with responsive crosslinks. Comptes Rendus Mécanique. 2014;342:264–272.

[24] Zhu L, Sun Y, Hess DW, et al. Well-aligned open-ended carbon nanotube architectures: an approach for device assembly. Nano Lett. 2006;6:243–247.

[25] De Volder MFL, Tawfick SH, Baughman RH, et al. Carbon Nanotubes: Present and Future Commercial Applications. Science. 2013;339:535–539.

[26] Zhang Q, Huang J-Q, Qian W-Z, et al. The Road for Nanomaterials Industry: A Review of Carbon Nanotube Production, Post-Treatment, and Bulk Applications for Composites and Energy Storage. Small. 2013;9:1237–1265.

[27] Lee YT, Park J, Choi YS, et al. Temperature-Dependent Growth of Vertically Aligned Carbon Nanotubes in the Range 800–1100 °C. J Phys Chem B. 2002;106:7614–7618.

[28] Choi G, Cho Y, Son K, et al. Mass production of carbon nanotubes using spin-coating of nanoparticles. Microelectronic Eng. 2003;66:77–82.

[29] Mahdavi M, Ahmad MB, Haron MJ, et al. Synthesis, surface modification and characterisation of biocompatible magnetic iron oxide nanoparticles for biomedical applications. Molecules. 2013;18:7533–7548.

[30] Sun J, Zhou S, Hou P, et al. Synthesis and characterization of biocompatible Fe3O4 nanoparticles. J Biomed Mater Res. 2007;80A:333–341.

[31] Herranz F, Salinas B, Groult H, et al. Superparamagnetic Nanoparticles for Atherosclerosis Imaging. Nanomaterials. 2014;4:408–438.

[32] Amiens C, Chaudret B, Ciuculescu-Pradines D, et al. Organometallic approach for the synthesis of nanostructures. New J Chem. 2013;37:3374–3401.

[33] Zhong Z, Lin M, Ng V, et al. A Versatile Wet-Chemical Method for Synthesis of One-Dimensional Ferric and Other Transition Metal Oxides. Chem Mater. 2006;18:6031–6036.

[34] Li Y, Afzaal M, O'Brien P. The synthesis of amine-capped magnetic (Fe, Mn, Co, Ni) oxide nanocrystals and their surface modification for aqueous dispersibility. J Mater Chem. 2006;16:2175–2180.

[35] Hou Y, Kondoh H, Ohta T, et al. Size-controlled synthesis of nickel nanoparticles. Appl Surf Sci. 2005;241:218–222.

[36] Shen L, Laibinis PE, Hatton TA. Bilayer Surfactant Stabilized Magnetic Fluids: Synthesis and Interactions at Interfaces. Langmuir. 1999;15:447–453.

[37] Wang H, Jiao X, Chen D. Monodispersed nickel nanoparticles with tunable phase and size: synthesis, characterization, and magnetic properties. J Phys Chem C. 2008;112:18793–18797.

[38] Yang JJ, Cheng H, Frost RL. Synthesis and characterisation of cobalt hydroxy carbonate Co 2 CO 3 (OH) 2 nanomaterials. Spectrochimica Acta Part A: Mol Biomol Spectroscopy. 2011;78:420–428.

[39] Mishra T, Sahu RK, Lim SH, et al. Hexadecylamine capped silver and gold nanoparticles: Comparative study on formation and self-organization. Mat Chem Phys. 2010;123:540–545.

[40] Newman JDS, Blanchard GJ. Formation of gold nanoparticles using amine reducing agents. Langmuir. 2006;22:5882–5887.

[41] Hou X, Zhang X, Fang Y, et al. 1-Hexadecylamine as both reducing agent and stabilizer to synthesize Au and Ag nanoparticles and their SERS application. J Nanopart Res. 2011;13:1929–1936.

[42] Yang H, Shen C, Wang Y, et al. Stable cobalt nanoparticles passivated with oleic acid and triphenylphosphine. Nanotechnol. 2004;15:70.

[43] Mohapatra J, Mitra A, Bahadur D, et al. Surface controlled synthesis of MFe2O4(M = Mn, Fe, Co, Ni and Zn) nanoparticles and their magnetic characteristics. Cryst Eng Comm. 2013;15:524–532.

[44] Zhao S-Y, Lee DK, Kim CW, et al. Synthesis of magnetic nanoparticles of Fe3O4 and CoFe2O4 and their surface modification by surfactant adsorption. Bulletin Korean Chemical Soc. 2006;27:237–242.

[45] Roy D, Ram K. Magnetite nanoparticles by organic-phase synthetic route for carbon nanotube growth. Synthetic Metals. 2009;159:343–346.

[46] Cao LF, Xu GY, Xie D, et al. Thermal stability of Fe, Co, Ni metal nanoparticles. Physica Status Solidi (b). 2006;243(12):2745–2755.

[47] Ahmadzade F, Safa S, Balashabady P. Growth of Vertically Aligned Carbon Nanotubes by DCPECVD System and the Effects of C2H2 Concentration and Plasma Current on the Growth Behavior of CNTs. Arab J Sci Eng. 2011;36:97–103.

[48] Wang H, Moore JJ. Low temperature growth mechanisms of vertically aligned carbon nanofibers and nanotubes by radio frequency-plasma enhanced chemical vapor deposition. Carbon. 2012;50:1235–1242.

[49] Ren ZF, Huang ZP, Xu JW, et al. Synthesis of large arrays of well-aligned carbon nanotubes on glass. Sci (Washington, D C). 1998;282:1105–1107.

[50] Somers W, Bogaerts A, van Duin ACT, et al. Interactions of plasma species on nickel catalysts: A reactive molecular dynamics study on the influence of temperature and surface structure. Appl Catal B: Environ. 2014;154–155:1–8.

[51] Chen HL, Lee HM, Chen SH, et al. Review of plasma catalysis on hydrocarbon reforming for hydrogen production-Interaction, integration, and prospects. Appl Catal B: Environ. 2008;85:1–9.

[52] Chen M, Chen C-M, Shi S-C, et al. Low-temperature synthesis multiwalled carbon nanotubes by microwave plasma chemical vapor deposition using CH4-CO2 gas mixture. Jpn J Appl Phys. 2003;42:614–619.

[53] Maschmann MR, Amama PB, Goyal A, et al. Freestanding vertically oriented single-walled carbon nanotubes synthesized using microwave plasma-enhanced CVD. Carbon. 2006;44:2758–2763.

[54] Dai H. Carbon nanotubes: opportunities and challenges. Surf Sci. 2002;500:218–2141.

[55] Kim NS, Bae SY, Park J. The catalytic effect on vertically aligned carbon nanotubes. Mater Res Soc Symp Proc. 2003;800:105–110.

[56] Altavilla C, Leone C, Sannino D, et al. Synthesis of monodispersed MFe2O4 (M = Fe, Co, Ni) ferrite nanoparticles: effect of reaction temperature on particle size. In: Nanotechnology 2009: Fabrication, Particles, Characterization, MEMS, Electronics and Photonics - Technical Proceedings of the 2009 NSTI Nanotechnology Conference and Expo, NSTI-Nanotech. 2009. p. 143–146.

[57] Raravikar NR, Schadler LS, Vijayaraghavan A, et al. Synthesis and characterization of thickness-aligned carbon nanotube-polymer composite films. Chem Mater. 2005;17:974–983.

[58] Casillas PEG, Gonzalez CAR, Pérez CAM. Infrared Spectroscopy of Functionalized Magnetic Nanoparticles, Infrared Spectroscopy – Materials Science, Engineering and Technology. In: Prof. Theophanides T, editor. InTech; 2012. Available from: https://www.intechopen.com/books/infrared-spectroscopy-materials-science-engineering-and-technology/infrared-spectroscopy-of-functionalized-magnetic-nanoparticles

[59] Dupuis A-C. The catalyst in the CCVD of carbon nanotubes—a review. Prog Mat Sci. 2005;50:929–961.

[60] Costa S, Borowiak-Palen E, Kruszynska M, et al. Characterization of carbon nanotubes by Raman spectroscopy. Mater Sci-Poland. 2008;26:433–41.

[61] Günes S, Neugebauer H, Sariciftci NS. Conjugated polymer-based organic solar cells. Chem Rev. 2007;107:1324–1338.

[62] van de Lagemaat J, Barnes TM, Rumbles G, et al. Organic solar cells with carbon nanotubes replacing In[sub 2]O[sub 3]:Sn as the transparent electrode. Appl Phys Lett. 2006;88:233503.